Observation of two types of fractional excitations in the Kitaev honeycomb magnet

Nejc Janša,[1] Andrej Zorko,[1] Matjaž Gomilšek,[1] Matej Pregelj,[1] Karl W. Krämer,[2] Daniel Biner,[2] Alun Biffin,[3] Christian Rüegg,[3,4] and Martin Klanjšek[1,*]

[1] *Jožef Stefan Institute, Jamova 39, 1000 Ljubljana, Slovenia*
[2] *Department of Chemistry and Biochemistry, University of Bern, CH-3012 Bern, Switzerland*
[3] *Laboratory for Neutron Scattering and Imaging, Paul Scherrer Institut, CH-5232 Villigen, Switzerland*
[4] *Department of Quantum Matter Physics, University of Geneva, CH-1211 Geneva, Switzerland*

(Dated: March 19, 2018)

Quantum spin liquid is a disordered, but highly entangled magnetic state with fractional spin excitations [1]. The ground state of an exactly solved Kitaev honeycomb model is perhaps its clearest example [2]. Under a magnetic field, a spin flip in this model fractionalizes into two types of anyons, quasiparticles with more complex exchange statistics than standard fermions or bosons: a pair of gauge fluxes and a Majorana fermion [2, 3]. Here we demonstrate this kind of fractionalization in the Kitaev paramagnetic state of the honeycomb magnet α-$RuCl_3$. The spin-excitation gap determined by nuclear magnetic resonance consists of the predicted Majorana fermion contribution following the cube of the applied magnetic field [2, 4, 5], and a finite zero-field contribution matching the predicted size of the gauge-flux gap [2, 6]. The observed fractionalization into gapped anyons survives in a broad range of temperatures and magnetic fields, which establishes α-$RuCl_3$ as a unique platform for future investigations of anyons.

In many-body systems dominated by strong fluctuations, an excitation with a well defined quantum number can break up into exotic quasiparticles with fractional quantum numbers. Well known examples include fractionally charged quasiparticles in fractional quantum Hall effect [7], spin-charge separation in one-dimensional conductors [8], and magnetic monopoles in spin ice [9]. A major hunting ground for novel fractional quasiparticles are disordered magnetic states of interacting spin-1/2 systems governed by strong quantum fluctuations, called quantum spin liquids (QSLs). Most of their models predict that a spin-flip excitation fractionalizes into a pair of spinons, each carrying spin 1/2 [1]. Even more interesting in this respect is the Kitaev model [2] of $S = 1/2$ spins on a two-dimensional (2D) honeycomb lattice with nearest neighbors interacting through an Ising exchange, whose axis depends on the bond direction, as shown in Fig. 1a. This is one of a few exactly solved 2D models supporting a QSL ground state. According to the solution, a spin flip fractionalizes into a pair of gauge fluxes and a Majorana fermion [2, 3]. As both types of quasiparticles behave as anyons under the magnetic field, they could potentially be used for decoherence-free topological quantum computation [2]. The experimental detection of such anyons is thus the primary goal of current QSL research.

As fractional quasiparticles are always created in groups, their common signature is a continuous spin-excitation spectrum, observed in recent QSL candidates on the kagome and triangular lattices [10, 11], instead of sharp magnon modes found in ordered magnets. A Kitaev QSL also exhibits this feature [6, 12], as well as additional, specific signatures, all related to the fact that fractionalization in this case leads to different quasiparticles. First, the fractionalization proceeds in two steps, with both types of quasiparticles releasing their entropy at different temperatures [13]. Second, although Majorana fermions themselves are gapless in zero magnetic field, the response of the QSL to a spin flip is gapped due to the inevitable simultaneous creation of a pair of gapped gauge fluxes [6]. And third, in the presence of an external magnetic field, the Majorana fermions also acquire a gap, which is predicted to grow with the characteristic third power of the field in the low-field region [2, 4, 5]. Currently, α-$RuCl_3$ is the most promising candidate for the realization of the Kitaev QSL [12, 14–17]. Among the listed signatures, a spin-excitation continuum was observed by Raman spectroscopy [12, 14] and inelastic neutron scattering [15–17], and the two-step thermal fractionalization was confirmed by specific-heat measurements [17], all in zero field. However, an application of a finite field, which should affect the gaps of both types of quasiparticles in different ways, is crucial to identify them. Using nuclear magnetic resonance (NMR), we determine the field dependence of the spin-excitation gap Δ shown in Fig. 1c, which indeed exhibits a finite zero-field value predicted for gauge fluxes and the cubic growth predicted for Majorana fermions. This result clearly demonstrates the fractionalization of a spin flip into two types of anyons in α-$RuCl_3$.

α-$RuCl_3$ is structurally related to the other two Kitaev QSL candidates, Na_2IrO_3 [18] and α-Li_2IrO_3 [19]. All three are layered Mott insulators based on the edge-sharing octahedral units, $RuCl_6$ and IrO_6 (Fig. 1a), respectively, and driven by strong spin-orbit coupling [20], which together lead to a dominant Kitaev exchange coupling between the effective $S = 1/2$ spins of Ru^{3+} and Ir^{4+} ions, respectively [21]. A monoclinic distortion of the IrO_6 octahedra in both iridate compounds results in the presence of non-Kitaev exchange interactions between the spins, which lead to the low-temperature mag-

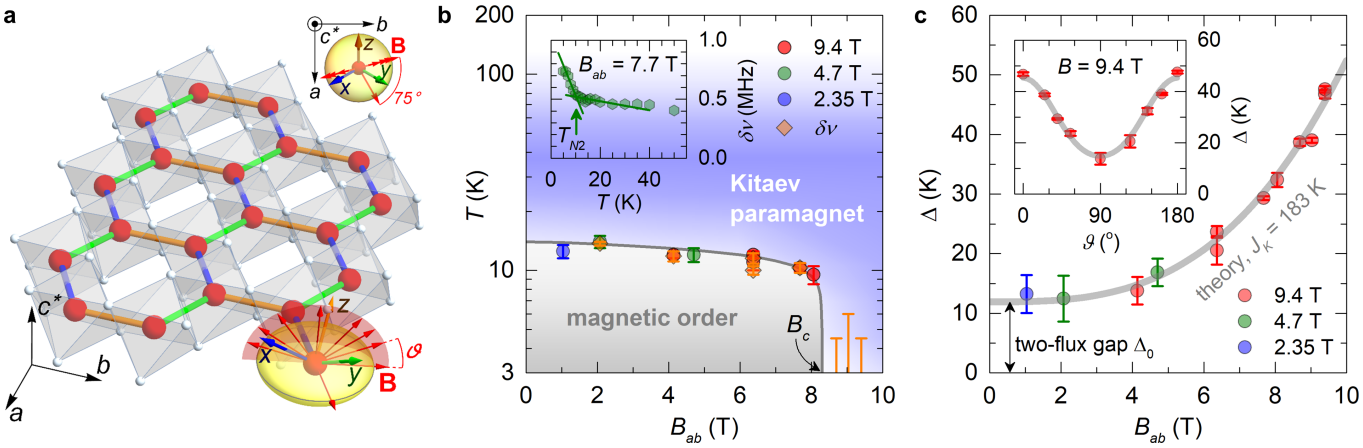

FIG. 1. **Structure of α-$RuCl_3$ and the key signature of anyons.** **a**, The structure of a single layer of α-$RuCl_3$ with the monoclinic $C2/m$ (no. 12) space group and monoclinic axis b ($c^* \perp a, b$). Spin-1/2 Ru^{3+} ions (red spheres) at the centers of the edge-sharing $RuCl_6$ octahedra (gray) form an almost perfect honeycomb lattice. Ising axes of the Kitaev exchange interactions between nearest-neighboring spins are perpendicular to the bond directions, pointing along x, y or z for blue, green and orange bonds, respectively. Red arrows show the employed magnetic field directions (described by the angle ϑ from the ab plane) with respect to the oblate Ru^{3+} g-tensor (yellow ellipsoid) of axial symmetry around c^*. The field directions form a fan (red semicircle) perpendicular to the ab plane, at 15° from the b axis (inset). **b**, Phase diagram of α-$RuCl_3$ as a function of temperature T and the effective magnetic field $B_{ab} = g(\vartheta)B/g_{ab}$ (so that $B_{ab} = B$ for $\vartheta = 0°$) for various values of B and ϑ. The boundary of the magnetically ordered phase extending up to $B_c \approx 8$ T, obtained from the ^{35}Cl linewidth $\delta\nu(T)$ (inset) and $T_1^{-1}(T)$ (Fig. 3), matches the result of Ref. [25] (gray line). The error bars represent one standard deviation. **c**, The spin-excitation gap Δ (obtained from fits in Fig. 3) as a function of B_{ab} follows the theoretically predicted cubic dependence given by Eq. (2) (gray line) with a finite zero-field offset (corresponding to the two-flux gap $\Delta_0 = 0.065J_K$ [6]) leading to $J_K = 183 \pm 10$ K. The error bars reflect the change of the determined Δ values upon adding or removing a single edge $T_1^{-1}(T)$ data point. Inset shows $\Delta(\vartheta)$ for $B = 9.4$ T together with the curve obtained from the theoretically predicted $\Delta(B_{ab})$ (gray line). The only field direction outside the red fan in **a** is assigned $\vartheta = 180°$.

netic ordering and thus prevent the realization of the QSL ground state. Judging by the lower transition temperature with respect to the Kitaev exchange coupling J_K, these interactions are smaller in α-$RuCl_3$ [22–24]. Signatures of fractional quasiparticles should be sought in a region of the phase diagram outside the magnetically ordered phase, at temperatures low enough that the Kitaev physics is not yet destroyed by thermal fluctuations. This is the Kitaev paramagnetic phase (Fig. 1b) extending to a relatively high temperature of around 100 K, roughly half of $J_K = 190$ K [17].

The boundary of the magnetically ordered phase measured in a large α-$RuCl_3$ single crystal (see Methods) using ^{35}Cl NMR is displayed in Fig. 1b. The magnetic response of α-$RuCl_3$ is known to be highly anisotropic [23, 25], mainly due to the anisotropic Ru^{3+} g-tensor (Fig. 1a) with $g_{ab} = 2.5$ and $g_{c^*} = 1.1$ [26]. Namely, the effect of an applied magnetic field $\mathbf{B}$ is described by the Zeeman term, which is proportional to $\underline{g}\mathbf{B}$ with magnitude $g(\vartheta)B$, where $\underline{g}$ is the g-tensor and $g(\vartheta) = \sqrt{g_{ab}^2 \cos^2\vartheta + g_{c^*}^2 \sin^2\vartheta}$ is the direction-dependent g-factor. Therefore, if $\mathbf{B}$ is applied at an angle ϑ from the ab plane, it produces the same effect as the field with magnitude $B_{ab} = g(\vartheta)B/g_{ab}$ applied in the ab plane. We exploit this to efficiently scan the phase diagram as a function of B_{ab} by varying both the direction and the magnitude of an applied field, instead of varying only the magnitude of a field applied in the ab plane, as is usually done [25]. This approach is valid if the g-tensor is the only source of anisotropy, a condition to be verified at the end (Fig. 1c). As shown in the inset of Fig. 1b, we determine the transition temperature T_{N2} as the onset of NMR line broadening (see Methods) monitored on the dominant NMR peak (inset of Fig. 2d). The obtained phase boundary extending up to the critical field $B_c \approx 8$ T matches the result of a recent reference study [25]. The observed transition temperature T_{N2} of around 14 K near zero field is consistent with a considerable presence of the two-layer AB stacking in the monoclinic $C2/m$ crystal structure (Fig. 1a), in addition to the three-layer ABC stacking, which is characterized by a lower transition temperature T_{N1} of around 7 K in zero field [15, 24]. As our study is focused on the Kitaev paramagnetic region (Fig. 1b) governed by the physics of individual layers, it is not affected by the particular stacking type.

To detect and monitor the spin-excitation gap as a function of the magnetic field, we use the NMR spin-lattice relaxation rate T_1^{-1}, which directly probes the low-energy limit of the local spin-spin correlation function and thus offers a direct access to the spin-excitation

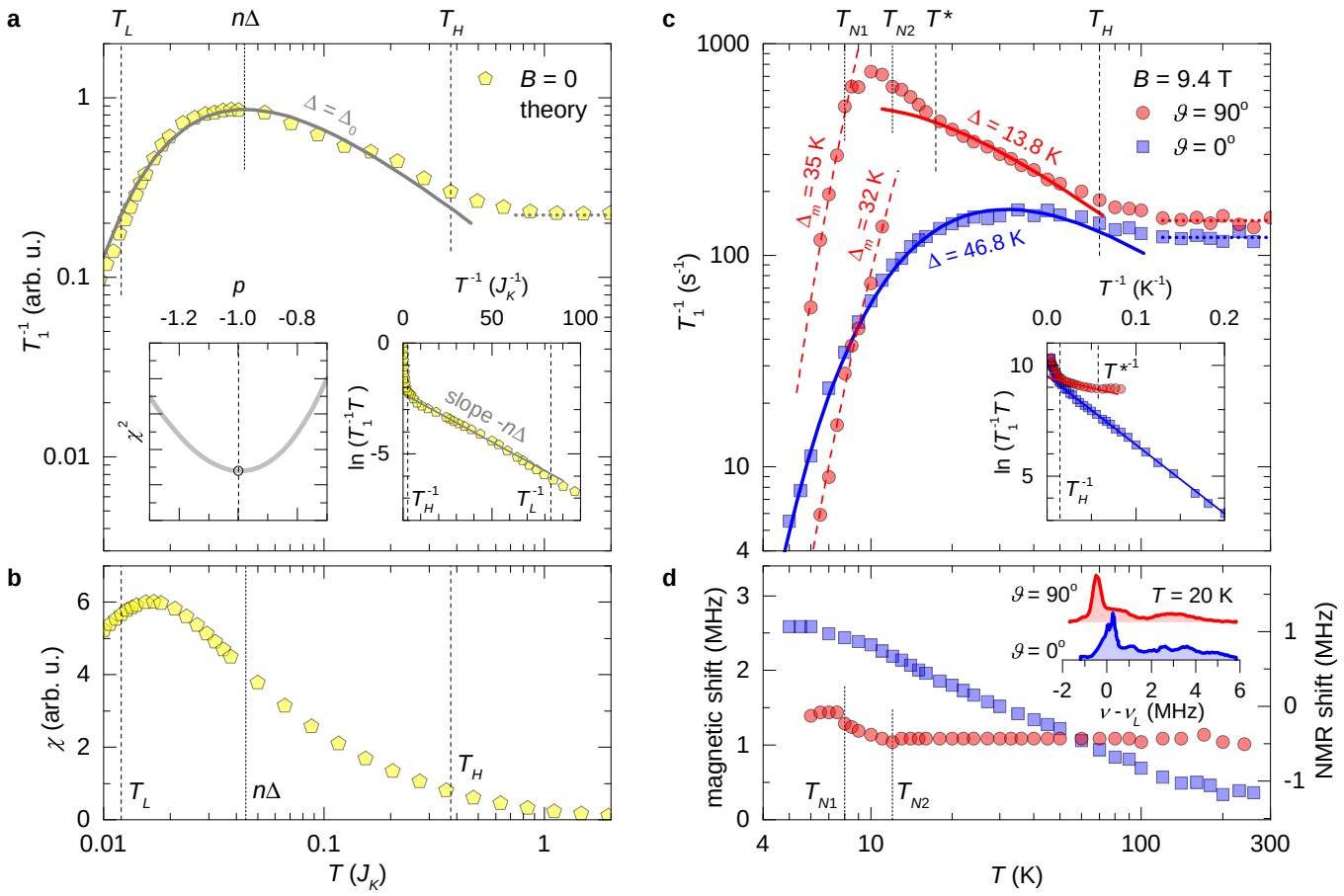

FIG. 2. **Signature of the Kitaev spin excitations. a,b**, T_1^{-1} and susceptibility χ as a function of temperature T theoretically calculated for the ferromagnetic Kitaev model in zero field [28] (see Methods). Dotted gray line is a temperature-independent fit in the classical paramagnetic phase. Solid gray line is a fit to Eq. (1) with $\Delta = \Delta_0 = 0.065J_K$ in the Kitaev paramagnetic phase between T_L and T_H leading to $n = 0.67$. First inset shows the goodness of the fit χ^2 as a function of p using the generalized form $T_1^{-1} \propto T^p \exp(n\Delta/T)$, where the minimum is almost exactly at $p = -1$ used in Eq. (1). Second inset demonstrates the resulting linear dependence of $\ln(T_1^{-1}T)$ on T^{-1} with the slope $-n\Delta$ between T_H^{-1} and T_L^{-1}. **c**, Temperature dependence of ^{35}Cl T_1^{-1} taken on the dominant NMR peak (inset of **d**) in 9.4 T for two magnetic field orientations, $\vartheta = 90°$ ($B_{ab} = 4.1$ T) and $\vartheta = 0°$ ($B_{ab} = 9.4$ T). The dataset for $\vartheta = 90°$ exhibits two transitions into magnetically ordered states, at $T_{N2} = 12$ K (AB stacking) and at $T_{N1} = 8$ K (ABC stacking). Dashed red lines are fits to $T_1^{-1} \propto T^2 \exp(-\Delta_m/T)$ for gapped magnon excitations in the 3D magnetically ordered state. Dotted blue and red lines are temperature-independent fits in the classical paramagnetic phase (see Methods). Solid blue and red lines are fits to Eq. (1) with $n = 0.67$ for Kitaev spin excitations up to $T_H \approx 70$ K (and down to $T^* \approx 17$ K for $\vartheta = 90°$, see Methods). Inset demonstrates the linear dependence of $\ln(T_1^{-1}T)$ on T^{-1} (obtained from Eq. (1)) in the appropriate T^{-1} range. **d**, Temperature dependent ^{35}Cl magnetic shift (i.e., NMR shift with subtracted quadrupole shift, see Methods) of the dominant NMR peak (inset shows the whole central line) in 9.4 T for two field orientations. The dataset for $\vartheta = 0°$ increases on cooling, approaching the maximum at 5 K, in accordance with the theoretical result in **b** where the maximum is reached at $0.017J_K \approx 3.2$ K. The dataset for $\vartheta = 90°$ is almost temperature-independent down to T_{N2}, in line with the temperature dependence of susceptibility for $\vartheta = 90°$ [22].

gap. Fig. 2a shows an exact theoretical $T_1^{-1}(T)$ dependence numerically calculated for the ferromagnetic Kitaev model in zero field [27, 28] adapted to the case of α-$RuCl_3$ (see Methods). It is dominated by a broad maximum, which is a sign of thermally excited pairs of gauge fluxes over the two-flux gap [27], whose exact value amounts to $\Delta_0 = 0.065J_K$ [2, 6]. The Kitaev paramagnetic phase is located between $T_L = 0.012J_K$, where gapped gauge fluxes start to be excited, and $T_H = 0.375J_K$, where thermal fluctauations already destroy the short-range spin correlations [13, 27]. As shown in Fig. 2a, in this broad temperature range, the theoretical zero-field $T_1^{-1}(T)$ dataset can be nicely reproduced with the empirical expression

$$T_1^{-1} \propto \frac{1}{T} \exp\left(-\frac{n\Delta}{T}\right), \qquad (1)$$

where Δ is the field-dependent spin-excitation gap, and the fitting procedure gives $n = 0.67$ when setting $\Delta = \Delta_0$

for zero field. In the following, we use Eq. (1) with this value of n to extract the gap Δ from the experimental $T_1^{-1}(T)$ datasets. Due to the unusual prefactor T^{-1} on the right-hand side of Eq. (1), Δ is encoded in the specific concave shape of the curve with the maximum at a temperature $n\Delta$. As shown in the second inset of Fig. 2a, the gap is also directly accessible from the negative slope $-n\Delta$ of the linear dependence of $\ln(T_1^{-1}T)$ on T^{-1}.

A broad maximum characteristic of the Kitaev spin excitations indeed appears in the ^{35}Cl $T_1^{-1}(T)$ dataset recorded in 9.4 T for the magnetic field orientation $\vartheta = 0°$ ($B_{ab} = 9.4$ T), as shown in Fig. 2c. The dataset is excellently reproduced with Eq. (1) using $\Delta = 46.8$ K in the temperature range up to $T_H = 0.375J_K \approx 70$ K for $J_K = 190$ K [17]. In the $T_1^{-1}(T)$ dataset for $\vartheta = 90°$ ($B_{ab} = 4.1$ T), a maximum would apparently develop at a lower temperature, if the dataset was not disrupted by a magnetic ordering transition at $T_{N2} = 12$ K (Fig. 2c). Between $T^* \approx 17$ K, where the critical fluctuations preceding the magnetic ordering vanish (see Methods and Supplementary Information), and T_H, the dataset is perfectly reproduced with Eq. (1) using $\Delta = 13.8$ K. A large difference between the two determined gaps in Fig. 2c points to a significant $\Delta(B_{ab})$ variation in the Kitaev paramagnetic phase. Below T_{N2}, two T_1^{-1} components develop, both exhibiting a steep drop, one below T_{N2} and the other one below $T_{N1} = 8$ K. These two phase transitions were observed before and ascribed to the presence of AB and ABC stackings, respectively [15, 24]. Fitting the data below T_{N2} and T_{N1} with the expression $T_1^{-1} \propto T^2 \exp(-\Delta_m/T)$ valid for gapped magnon excitations in a 3D magnetically ordered state (see Methods) gives comparable values of the magnon gap $\Delta_m = 32$ K and 35 K, respectively, implying the same low-energy physics in both cases. The obtained values are consistent with the gap of 29 K determined by inelastic neutron scattering [15, 29]. Finally, the temperature-independent part of both $T_1^{-1}(T)$ datasets above 120 K ($\approx 2T_H$) indicates a crossover into a classical paramagnetic state (see Methods), in accordance with the theoretical dataset in Fig. 2a and with the experimental result of Ref. [17].

Although Eq. (1) is empirical, its functional form already bears signs of the involved fractional spin excitations. To show this, we first note that similar expressions are obtained for more conventional gapped magnon excitations in magnetic insulators at low temperatures $T \ll \Delta$ (see Methods). In that case, the prefactor T^{-1} is replaced by a more general T^p originating from the magnon density of states $g(E)$, which depends on the dimensionality D, while n is generally the number of magnons involved in the process. For $n = 1$ (single-magnon scattering) and a quadratic dispersion relation for magnons, one obtains $p = D - 1 \geq 0$, while higher n (multi-magnon scattering) lead to even higher powers p (see Methods). At higher temperatures $T \sim \Delta$, the effective p changes, but always remains positive. Therefore, a very unusual, theoretically confirmed $p = -1$ in Eq. (1) valid over a broad temperature range cannot be obtained for magnons. This, together with a fractional number $n = 0.67$ of the involved spin-flip excitations obtained in Fig. 2a, indicates that Eq. (1) is actually specific to the presence of fractional spin excitations.

In the ferromagnetic Kitaev model, the magnetic susceptibility χ exhibits a moderate, almost monotonic temperature dependence (Fig. 2b), in contrast to the non-monotonic $T_1^{-1}(T)$ behavior (Fig. 2a) [27, 28]. As shown in Figs. 2c,d, we indeed observe contrasting temperature dependencies of T_1^{-1} and the local susceptibility monitored by the ^{35}Cl NMR shift in 9.4 T for $\vartheta = 0°$. While both observables should exhibit a similar gapped behavior in the presence of gapped magnon excitations, such a contrast between them can only arise in the presence of at least two types of fractional quasiparticles that enter the two observables in different ways [27].

To obtain the spin-excitation gap Δ as a function of B_{ab} in Fig. 1c, the $T_1^{-1}(T)$ datasets in Fig. 3 taken in magnetic fields of different directions and magnitudes are fitted to Eq. (1) in the temperature range of the Kitaev paramagnetic phase. As the curve $T_1^{-1} \propto T^{-1}$ defined by $\Delta = 0$ is steeper than any dataset in this range or, equivalently, as the datasets in the insets of Fig. 3 all exhibit a negative slope in this range, the obtained excitation gaps are obviously all finite. The inset of Fig. 1c showing the symmetric $\Delta(\vartheta)$ dependence around 90° in 9.4 T, where ϑ traverses nonequivalent directions with respect to the Ising axes on both sides (inset of Fig. 1a), demonstrates that the g-tensor is indeed the only source of anisotropy as assumed when introducing B_{ab}. The obtained $\Delta(B_{ab})$ in Fig. 1c can be perfectly reproduced as a sum of two terms: the two-flux gap $\Delta_0 = 0.065J_K$ [2, 6] and the gap acquired by Majorana fermions in a weak magnetic field, theoretically predicted to be proportional to the cube of the field [2, 4, 5] (see Methods),

$$\Delta = \Delta_0 + \alpha \frac{\widetilde{B}^3}{\Delta_0^2}, \tag{2}$$

where $\widetilde{B} = g_{ab}\mu_B B_{ab}/k_B$ is the field in kelvin units, k_B is the Boltzmann constant, μ_B the Bohr magneton and α accounts for the sum over the excited states in the third-order perturbation theory, which is the origin of the $\widetilde{B}^3$ term [2]. The fitting procedure leads to $\alpha = 1.2$ and $J_K = 183 \pm 10$ K, in perfect agreement with the value of 190 K determined by inelastic neutron scattering [17]. This result demonstrates that a spin-flip excitation in α-$RuCl_3$ indeed fractionalizes into a gauge-flux pair and a Majorana fermion.

Focusing on the low-field Kitaev paramagnetic region in the phase diagram of α-$RuCl_3$ in Fig. 1b is essential for our identification of two types of anyons. Instead, other recent experimental studies focused on the low-temperature region above B_c, observing the spin-

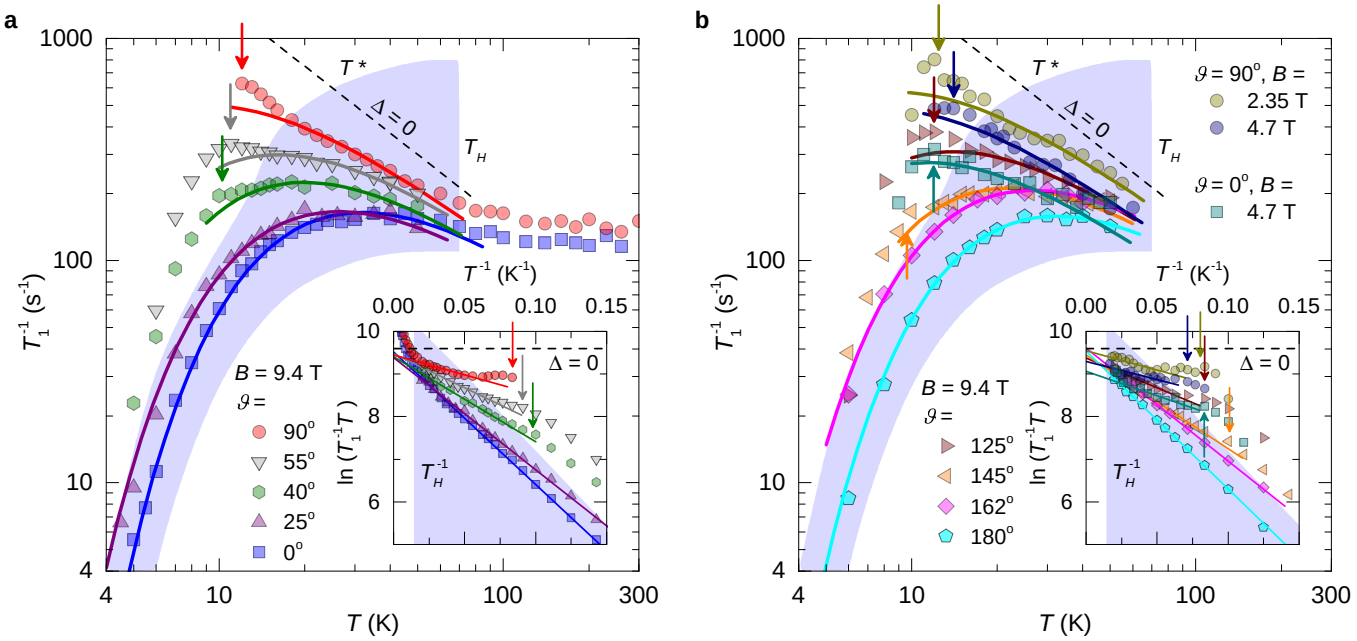

FIG. 3. **Determination of the spin-excitation gap Δ. a,b**, ^{35}Cl T_1^{-1} as a function of temperature T in 2.35, 4.7 and 9.4 T for various magnetic field orientations given by ϑ. Arrows mark the transition temperatures T_{N2} into the magnetically ordered state, determined by a weakly pronounced onset of a T_1^{-1} decrease on decreasing T. Solid lines are fits to Eq. (1) with $n = 0.67$ for Kitaev spin excitations between T^*, where the critical fluctuations related to magnetic ordering vanish, and $T_H = 70$ K (blue background). These allow us to determine $\Delta(\vartheta)$ and $\Delta(B_{ab})$ dependencies shown in Fig. 1c. Dashed lines are the curves $T_1^{-1} \propto T^{-1}$ defined by $\Delta = 0$ exhibiting the largest negative slope. Insets demonstrate the linear dependence of $\ln(T_1^{-1}T)$ on T^{-1} (obtained from Eq. (1)) in the appropriate T^{-1} range (blue background). Dashed horizontal lines correspond to $\Delta = 0$.

excitation continuum [30] with either a gapless behavior [31] or the gap opening linearly [32–35] or sublinearly [36] with $B - B_c$, but without definite conclusions about the identity of the involved quasiparticles. These contradicting conclusions likely originate from the presence of additional, non-Kitaev interactions between the spins [15, 26, 29, 37], whose role should be pronounced particularly at low temperatures. Our result shows that spin fractionalization into two types of anyons is robust against these interactions in a broad range of temperatures and magnetic fields. This is the main practical advantage of α-$RuCl_3$ with respect to all other anyon realizations, such as the fractional quantum Hall effect in 2D heterostructures [7] or hybrid nanowire devices [38], where anyons are observed only at extremely low temperatures and for certain field values. Our discovery thus establishes α-$RuCl_3$ as a unique platform for future investigations of anyons.

* martin.klanjsek@ijs.si

[1] L. Savary and L. Balents, Quantum spin liquids: a review, *Rep. Prog. Phys.* **80**, 016502 (2017).
[2] A. Kitaev, Anyons in an exactly solved model and beyond, *Ann. Phys.* **321**, 2-111 (2006).
[3] G. Baskaran, S. Mandal, and R. Shankar, Exact Results for Spin Dynamics and Fractionalization in the Kitaev Model, *Phys. Rev. Lett.* **98**, 247201 (2007).
[4] H.-C. Jiang, Z.-C. Gu, X.-L. Qi, and S. Trebst, Possible proximity of the Mott insulating iridate Na_2IrO_3 to a topological phase: Phase diagram of the Heisenberg-Kitaev model in a magnetic field, *Phys. Rev. B* **83**, 245104 (2011).
[5] J. Nasu, J. Yoshitake, and Y. Motome, Thermal Transport in the Kitaev Model, *Phys. Rev. Lett.* **119**, 127204 (2017).
[6] J. Knolle, D. L. Kovrizhin, J. T. Chalker, and R. Moessner, Dynamics of a two-dimensional quantum spin liquid: signatures of emergent Majorana fermions and fluxes, *Phys. Rev. Lett.* **112**, 207203 (2014).
[7] R. de-Picciotto, M. Reznikov, M. Heiblum, V. Umansky, G. Bunin, and D. Mahalu, Direct observation of a fractional charge, *Nature* **389**, 162-164 (1997).
[8] Y. Jompol, C. J. B. Ford, J. P. Griffiths, I. Farrer, G. A. C. Jones, D. Anderson, D. A. Ritchie, T. W. Silk, and A. J. Schofield, Probing Spin-Charge Separation in a Tomonaga-Luttinger Liquid, *Science* **325**, 597-601 (2009).
[9] C. Castelnovo, R. Moessner, and S. L. Sondhi, Magnetic monopoles in spin ice, *Nature* **451**, 42-45 (2008).
[10] T.-H. Han, J. S. Helton, S. Chu, D. G. Nocera, J. A. Rodriguez-Rivera, C. Broholm, and Y. S. Lee, Fractionalized excitations in the spin-liquid state of a kagome-lattice antiferromagnet, *Nature* **492**, 406-410 (2012).
[11] J. A.M. Paddison, M. Daum, Z. Dun, G. Ehlers, Y. Liu, M.B. Stone, H. Zhou, and M. Mourigal, Continuous excitations of the triangular-lattice quantum spin liquid $YbMgGaO_4$, *Nature Phys.* **13**, 117-122 (2017).

[12] J. Nasu, J. Knolle, D.L. Kovrizhin, Y. Motome, and R. Moessner, Fermionic response from fractionalization in an insulating two-dimensionalmagnet, *Nature Phys.* **12**, 912-915 (2016).

[13] J. Nasu, M. Udagawa, and Y. Motome, Thermal fractionalization of quantum spins in a Kitaev model: Temperature-linear specific heat and coherent transport of Majorana fermions, *Phys. Rev. B* **92**, 115122 (2015).

[14] L. J. Sandilands, Y. Tian, K. W. Plumb, Y.-J. Kim, and K. S. Burch, Scattering Continuum and Possible Fractionalized Excitations in α-$RuCl_3$, *Phys. Rev. Lett.* **114**, 147201 (2015).

[15] A. Banerjee, C. A. Bridges, J.-Q. Yan, A. A. Aczel, L. Li, M. B. Stone, G. E. Granroth, M. D. Lumsden, Y. Yiu, J. Knolle, S. Bhattacharjee, D. L. Kovrizhin, R. Moessner, D. A. Tennant, D. G. Mandrus, and S. E. Nagler, Proximate Kitaev quantum spin liquid behaviour in a honeycomb magnet, *Nature Mat.* **15**, 733-740 (2016).

[16] A. Banerjee, J. Yan, J. Knolle, C. A. Bridges, M. B. Stone, M. D. Lumsden, D. G. Mandrus, D. A. Tennant, R. Moessner, and S. E. Nagler, Neutron scattering in the proximate quantum spin liquid α-$RuCl_3$, *Science* **356**, 1055-1059 (2017).

[17] S.-H. Do, S.-Y. Park, J. Yoshitake, J. Nasu, Y. Motome, Y. S. Kwon, D. T. Adroja, D. J. Voneshen, K. Kim, T.-H. Jang, J.-H. Park, K.-Y. Choi, and S. Ji, Majorana fermions in the Kitaev quantum spin system α-$RuCl_3$, *Nature Phys.*, **13**, 1079-1084 (2017).

[18] S. K. Choi, R. Coldea, A. N. Kolmogorov, T. Lancaster, I. I. Mazin, S. J. Blundell, P. G. Radaelli, Yogesh Singh, P. Gegenwart, K. R. Choi, S.-W. Cheong, P. J. Baker, C. Stock, and J. Taylor, Spin Waves and Revised Crystal Structure of Honeycomb Iridate Na_2IrO_3, *Phys. Rev. Lett.* **108**, 127204 (2012).

[19] Y. Singh, S. Manni, J. Reuther, T. Berlijn, R. Thomale, W. Ku, S. Trebst, and P. Gegenwart, Relevance of the Heisenberg-Kitaev Model for the Honeycomb Lattice Iridates A_2IrO_3, *Phys. Rev. Lett.* **108**, 127203 (2012).

[20] K. W. Plumb, J. P. Clancy, L. J. Sandilands, V. V. Shankar, Y. F. Hu, K. S. Burch, H.-Y. Kee, and Y.-J. Kim, α-$RuCl_3$: A spin-orbit assisted Mott insulator on a honeycomb lattice, *Phys. Rev. B* **90**, 041112(R) (2014).

[21] G. Jackeli and G. Khaliullin, Mott insulators in the strong spin-orbit coupling limit: from Heisenberg to a quantum compass and Kitaev models, *Phys. Rev. Lett.* **102**, 017205 (2009).

[22] Y. Kubota, H. Tanaka, T. Ono, Y. Narumi, and K. Kindo, Successive magnetic phase transitions in α-$RuCl_3$: XY-like frustrated magnet on the honeycomb lattice, *Phys. Rev. B* **91**, 094422 (2015).

[23] M. Majumder, M. Schmidt, H. Rosner, A. A. Tsirlin, H. Yasuoka, and M. Baenitz, Anisotropic Ru^{3+} $4d^5$ magnetism in the α-$RuCl_3$ honeycomb system: Susceptibility, specific heat, and zero-field NMR, *Phys. Rev. B* **91**, 180401(R) (2015).

[24] H. B. Cao, A. Banerjee, J.-Q. Yan, C. A. Bridges, M. D. Lumsden, D. G. Mandrus, D. A. Tennant, B. C. Chakoumakos, and S. E. Nagler, Low-temperature crystal and magnetic structure of α-$RuCl_3$, *Phys. Rev. B* **93**, 134423 (2016).

[25] R. D. Johnson, S. C. Williams, A. A. Haghighirad, J. Singleton, V. Zapf, P. Manuel, I. I. Mazin, Y. Li, H. O. Jeschke, R. Valentí, and R. Coldea, Monoclinic crystal structure of α-$RuCl_3$ and the zigzag antiferromagnetic ground state, *Phys. Rev. B* **92**, 235119 (2015).

[26] R. Yadav, N. A. Bogdanov, V. M. Katukuri, S. Nishimoto, J. van den Brink, and L. Hozoi, Kitaev exchange and field-induced quantum spin-liquid states in honeycomb α-$RuCl_3$, *Sci. Rep.* **6**, 37925 (2016).

[27] J. Yoshitake, J. Nasu, and Y. Motome, Fractional Spin Fluctuations as a Precursor of Quantum Spin Liquids: Majorana Dynamical Mean-Field Study for the Kitaev Model, *Phys. Rev. Lett.* **117**, 157203 (2016).

[28] J. Yoshitake, J. Nasu, and Y. Motome, Temperature evolution of spin dynamics in two- and three-dimensional Kitaev models: Influence of fluctuating Z_2 flux, *Phys. Rev. B* **96**, 064433 (2017).

[29] K. Ran, J. Wang, W. Wang, Z.-Y. Dong, X. Ren, S. Bao, S. Li, Z. Ma, Y. Gan, Y. Zhang, J. T. Park, G. Deng, S. Danilkin, S.-L. Yu, J.-X. Li, and J. Wen, Spin-Wave Excitations Evidencing the Kitaev Interaction in Single Crystalline α-$RuCl_3$, *Phys. Rev. Lett.* **118**, 107203 (2017).

[30] A. Banerjee, P. Lampen-Kelley, J. Knolle, C. Balz, A. A. Aczel, B. Winn, Y. Liu, D. Pajerowski, J.-Q. Yan, C. A. Bridges, A. T. Savici, B. C. Chakoumakos, M. D. Lumsden, D. A. Tennant, R. Moessner, D. G. Mandrus, and S. E. Nagler, Excitations in the field-induced quantum spin liquid state of α-$RuCl_3$, *npj Quantum Materials* **3**, 8 (2018).

[31] J. Zheng, K. Ran, T. Li, J. Wang, P. Wang, B. Liu, Z.-X. Liu, B. Normand, J. Wen, and W. Yu, Gapless Spin Excitations in the Field-Induced Quantum Spin Liquid Phase of α-$RuCl_3$, *Phys. Rev. Lett.* **119**, 227208 (2017).

[32] S.-H. Baek, S.-H. Do, K.-Y. Choi, Y. S. Kwon, A. U. B. Wolter, S. Nishimoto, J. van den Brink, and B. Büchner, Evidence for a Field-induced Quantum Spin Liquid in α-$RuCl_3$, *Phys. Rev. Lett.* **119**, 037201 (2017).

[33] J. A. Sears, Y. Zhao, Z. Xu, J. W. Lynn, and Y.-J. Kim, Phase diagram of α-$RuCl_3$ in an in-plane magnetic field, *Phys. Rev. B* **95**, 180411(R) (2017).

[34] R. Hentrich, A. U. B. Wolter, X. Zotos, W. Brenig, D. Nowak, A. Isaeva, T. Doert, A. Banerjee, P. Lampen-Kelley, D. G. Mandrus, S. E. Nagler, J. Sears, Y.-J. Kim, B. Büchner, and C. Hess, Unusual Phonon Heat Transport in α-$RuCl_3$: Strong Spin-Phonon Scattering and Field-Induced Spin Gap, *Phys. Rev. Lett.* **120**, 117204 (2018).

[35] A. N. Ponomaryov, E. Schulze, J. Wosnitza, P. Lampen-Kelley, A. Banerjee, J.-Q. Yan, C. A. Bridges, D. G. Mandrus, S. E. Nagler, A. K. Kolezhuk, and S. A. Zvyagin, Unconventional spin dynamics in the honeycomb-lattice material α-$RuCl_3$: High-field electron spin resonance studies, *Phys. Rev. B* **96**, 241107(R) (2017).

[36] A. U. B. Wolter, L. T. Corredor, L. Janssen, K. Nenkov, S. Schönecker, S.-H. Do, K.-Y. Choi, R. Albrecht, J. Hunger, T. Doert, M. Vojta, and B. Büchner, Field-induced quantum criticality in the Kitaev system α-$RuCl_3$, *Phys. Rev. B* **96**, 041405(R) (2017).

[37] S. M. Winter, Y. Li, H. O. Jeschke, and R. Valentí, Challenges in design of Kitaev materials: Magnetic interactions from competing energy scales, *Phys. Rev. B* **93**, 214431 (2016).

[38] V. Mourik, K. Zuo, S. M. Frolov, S. R. Plissard, E. P. A. M. Bakkers, and L. P. Kouwenhoven, Signatures of Majorana Fermions in Hybrid Superconductor-Semiconductor Nanowire Devices, *Science* **336**, 1003-1007 (2012).

Acknowledgements

M.K. acknowledges fruitful discussions with M. Horvatić and C. Berthier. The work was partly supported by the Slovenian ARRS program No. P1-0125 and project No. PR-07587.

Author contributions

M.K. conceived, designed and led the project. N.J. and M.K. performed the NMR experiments and analyzed the data. K.W.K. and D.B. grew the samples. A.B. performed the magnetic susceptibility measurements. All the authors discussed the results. M.K. wrote the paper with feedback from all the authors.

Competing financial interests

The authors declare no competing financial interests.

Methods

Crystal growth. Crystals of α-$RuCl_3$ were synthesized from anhydrous $RuCl_3$ (Strem Chemicals). The starting material was heated in vacuum to 200 °C for one day to remove volatile impurities. In the next step, the powder was sealed in a silica ampoule under vacuum and heated to 650 °C in a tubular furnace. The tip of the ampoule was kept at lower temperature and the material sublimed to the colder end during one week. Phase pure α-$RuCl_3$ (with a high-temperature phase of $C2/m$ crystal structure) was obtained as thin crystalline plates. The residual in the hot part of the ampoule was black RuO_2 powder. The purified α-$RuCl_3$ was sublimed for the second time in order to obtain bigger crystal plates. The phase and purity of the compounds was verified by powder X-ray diffraction. All handling of the material was done under strictly anhydrous and oxygen-free conditions in glove boxes or sealed ampoules. Special care has to be taken when the material is heated in sealed-off ampoules. If gas evolves from the material, this may result in the explosion of the ampoule.

Nuclear magnetic resonance. The ^{35}Cl nuclear magnetic resonance (NMR) experiments were performed on a foil-like α-$RuCl_3$ single crystal of approximate dimensions $5 \times 5 \times 0.1$ mm^3 in a continuous-flow cryostat allowing us to reach temperatures down to 4.2 K. When handling the sample, we took extreme care to minimize its exposure to air. A thin NMR coil tightly fitting the sample was made from a thin copper wire with 20-40 turns, depending on the required tuning frequency determined by the external magnetic field. The coil was covered with a mixture of epoxy and ZrO_2 powder, which was allowed to harden, in order to ensure the rigidity of the coil. The coil was then mounted on a teflon holder attached to a rotator, which allowed us to vary the orientation of the sample with respect to the external magnetic field. In order to reduce the noise of an already weak ^{35}Cl NMR signal, a consequence of the extremely broad ^{35}Cl NMR spectrum, we used a bottom-tuning scheme. With the output radio-frequency power of around 20 W, a typical $\pi/2$ pulse duration was 2 μs. The NMR signals were recorded using the standard spin-echo, $\pi/2 - \tau_d - \pi$ pulse sequence with a typical delay of $\tau_d = 70$ μs (much shorter than the spin-spin relaxation time T_2) between the $\pi/2$ and π pulses.

T_1 relaxation. The spin-lattice relaxation (i.e., T_1) experiment was carried out using an inversion recovery pulse sequence, $\varphi_i - \tau - \pi/2 - \tau_d - \pi$, with an inversion pulse $\varphi_i < \pi$ (suitable for broad NMR lines) and a variable delay τ before the read-out spin-echo sequence. The spin-lattice relaxation datasets were typically taken at 20 increasing values of τ. The datasets were analyzed using the model of magnetic relaxation for $I = 3/2$ spin, appropriate for ^{35}Cl, monitored on the central $-1/2 \longleftrightarrow 1/2$ transition:

$$m(\tau) = 1 - (1+s)\left[0.1\exp\left(-\frac{\tau}{T_1}\right) + 0.9\exp\left(-\frac{6\tau}{T_1}\right)\right], \quad (3)$$

where T_1 is the spin-lattice relaxation time and s is the inversion factor. In the region of the phase diagram outside the magnetically ordered phase (Fig. 1b), this expression reproduces the experimental relaxation curves perfectly. In the magnetically ordered phase, two T_1 components appear, and the relaxation curves are reproduced as a sum of two terms of the form given by Eq. (3). For instance, the temperature dependence of the corresponding two T_1 values for $B = 9.4$ T with $\vartheta = 90°$ is given in Fig. 2c. In cases where only a narrow temperature region below the transition was covered, the two components in the relaxation curves were hard to separate, and we used Eq. (3) with a stretched exponent instead.

Relation between orientation and field dependence of T_1. Using also the direction of the applied magnetic field (described by the angle ϑ from the crystal ab plane), in addition to its magnitude, in order to change the value of B_{ab}, allows us to cover low B_{ab} values, while keeping the applied magnetic field B high. This is beneficial for two reasons related to the strong quadrupole broadening of the ^{35}Cl NMR spectrum (inset of Fig. 2d and Supplementary Fig. S2): to minimize an already large NMR linewidth and to keep the Larmor frequency well above the quadrupole splitting, which is of the order of 10 MHz as concluded in the following. The validity of this approach is supported by the fact that $\Delta(B_{ab})$ data points for various angles ϑ and field values 2.35, 4.7 and 9.4 T in Fig. 1c all collapse onto a smooth experimental curve. The $\Delta(B_{ab})$ data points taken in lower fields obviously exhibit much larger error bars. Namely, the corresponding $T_1^{-1}(T)$ datasets in Fig. 3b are more

scattered than the datasets taken in 9.4 T despite a much longer averaging for noise reduction.

The boundary of the magnetically ordered phase. We measured the temperature dependence of the dominant ^{35}Cl NMR peak in magnetic fields of various magnitudes and various directions with respect to the crystal ab plane of the sample, thus covering various B_{ab} values. For $B_{ab} < 8$ T, the frequency width of the peak exhibits a clear kink as a function of temperature (inset of Fig. 1b and Supplementary Fig. S3), which indicates the onset of NMR line broadening at the phase transition into the magnetically ordered state. Plotting the temperature of the kink as a function of B_{ab} in the inset of Fig. 1b (and in the inset of Supplementary Fig. S3), we obtain the boundary of the magnetically ordered phase, which perfectly matches the result of the reference study [25].

Contributions to the NMR shift. The temperature dependence of the NMR frequency shift of the dominant NMR peak measured in 9.4 T with the field in the ab plane ($\vartheta = 0°$) is plotted in Fig. 2d and reproduced in Supplementary Fig. S4. To separate the magnetic contribution to the NMR shift from the temperature-independent quadrupole contribution, we plot the relative NMR shift (i.e., the NMR shift divided by the ^{35}Cl Larmor frequency $\nu_L = 39.18$ MHz) against the rescaled magnetic susceptibility χ_{ab} in the inset of Supplementary Fig. S4. In Ref. [25], an experimental ratio between the susceptibility χ of the powdered sample and the susceptibility χ_{ab} of the single crystal with a field applied in the ab plane is obtained as $(2 + r)/3$ with $r = 0.157$, leading to $\chi_{ab} = 3\chi/(2 + r)$. We use this empirical relation to evaluate $\chi_{ab}(T)$ from our field-cooled $\chi(T)$ dataset shown in Supplementary Fig. S1. As we did not measure susceptibility in high magnetic fields, we rely on the dataset taken in 1.0 T. This is valid in a broad temperature range, except at low temperatures where this dataset starts to deviate from the high-field susceptibility [22]. The relative shift is found to depend linearly on χ_{ab} up to $20 \cdot 10^{-3}$ emu/mol (inset of Supplementary Fig. S4), i.e., the NMR shift follows χ_{ab} down to 35 K (Supplementary Fig. S4). The proportionality constant 1.95 mol/emu between the relative shift and χ_{ab} translates to 1.09 T/μ_B. When further multiplied by the relevant g-factor, $g_{ab} = 2.5$, and divided by 2 (as each ^{35}Cl is coupled equally to two Ru^{3+} $S = 1/2$ spins), we obtain the component $A = 1.35$ T (in the ab plane) of the hyperfine coupling tensor between ^{35}Cl and the Ru^{3+} $S = 1/2$ spin. In addition, a zero-temperature relative shift -0.039, when multiplied by ν_L, gives the quadrupole shift $\Delta\nu_Q = -1.53$ MHz.

From the obtained quadrupole shift $\Delta\nu_Q$, we can estimate the quadrupole splitting ν_Q between the successive ^{35}Cl NMR transitions. For the case of an axially symmetric electric field gradient (EFG) tensor and the field applied at an angle ϑ' from the principal EFG axis v_{ZZ} with the largest EFG eigenvalue, the second-order quadrupole shift is given by $\Delta\nu_Q = -3\nu_Q^2(1 - \cos\vartheta'^2)(9\cos\vartheta'^2 - 1)/(16\nu_L)$ for the $I = 3/2$ nucleus [39]. As the axes of the EFG tensor are not known, we assume a typical tilt 45° of v_{ZZ} from c^*, so that $\vartheta' \sim 45°$. From the previously evaluated $\Delta\nu_Q$ we then obtain $\nu_Q \sim 14.2$ MHz. This is an estimate of the quadrupole splitting between the central ^{35}Cl NMR transition and the satellite transitions. We can thus conclude that the NMR peaks in the covered frequency range (inset of Fig. 2d and Supplementary Fig. S2) all belong to the central transition.

Justification for the onset temperature T^*. A simple estimate of the onset temperature T^* for the critical spin fluctuations preceding the magnetic ordering at T_{N2} can be obtained using a random phase approximation (RPA) to express the dynamic susceptibility χ of α-$RuCl_3$. As the pure Kitaev magnet does not magnetically order, the magnetic ordering of α-$RuCl_3$ is a consequence of additional non-Kitaev interactions. If we denote the effective coupling of all these additional interactions together by J', the RPA expression reads $\chi = \chi_1/(1 - J'\chi_1)$, where χ_1 is the dynamic susceptibility of a single Kitaev plane. As $T_1^{-1}(T)$ can be reasonably well approximated by a negative power law above T^* (as evident from the $\vartheta = 90°$ dataset in Fig. 2c, which is linear in a log-log scale), the same holds for χ_1, i.e., $\chi_1 = cT^{-r}$ with $r > 0$. A condition $J'\chi_1(T_N) = 1$ for the phase transition at T_N can then be written as $cJ'T_N^{-r} = 1$. This allows us to express J' with T_N, so that the deviation of the dynamic susceptibility from the pure Kitaev case can finally be written in the form

$$\frac{\chi}{\chi_1} = \left[1 - \left(\frac{T}{T_N}\right)^{-r}\right]^{-1} . \qquad (4)$$

The ratio χ/χ_1 diverges when approaching T_N from above and gradually drops to 1 with increasing temperature. The temperature scale for this drop is apparently determined by T_N, which leads to the characteristic estimate $T^* \approx T_N + T_N = 2T_N$ consistent with our experimental determination (see Supplementary Information). Precisely such values of T^* with respect to T_N are also experimentally found in systems of coupled spin chains or ladders, whose χ_1 exactly obey power-law temperature dependences [40, 41].

Theoretical $T_1^{-1}(T)$ for Kitaev spin excitations. The theoretical temperature dependence of T_1^{-1} is numerically calculated for the Kitaev model in zero field [27]. T_1^{-1} contains two contributions, one coming from a single fluctuating spin (i.e., on-site) and the other one coming from fluctuating nearest-neighboring (NN) spins in the Kitaev honeycomb lattice. As the ^{35}Cl nucleus in α-$RuCl_3$ is located at equal distances from the

closest two Ru^{3+} $S = 1/2$ spins (Fig. 1a), T_1^{-1} generally contains both contributions. We evaluate their relative weights for the case of a magnetic field applied along c^* (i.e., $\vartheta = 90°$) and assuming an isotropic hyperfine coupling A. A general expression for T_1^{-1} [42] can then be written as

$$T_1^{-1} = \frac{\gamma^2}{2}\int_{-\infty}^{\infty} \mathrm{d}t \left\{ A^2 \Big\langle \big[S_1^a(t) + S_2^a(t)\big]\,(S_1^a + S_2^a)\Big\rangle + \right. \\ \left. + A^2 \Big\langle \big[S_1^b(t) + S_2^b(t)\big]\,(S_1^b + S_2^b)\Big\rangle \right\}, \quad (5)$$

where t is time, while S_1 and S_2 are the two involved Ru^{3+} $S = 1/2$ spins with relevant components perpendicular to the field direction, i.e., along a and b (Fig. 1a). In the orthogonal system defined by the Ising axes x, y and z (Fig. 1a), unit vectors along a, b and c^* are written as

$$\hat{e}_a = \frac{1}{\sqrt{6}}\begin{bmatrix} 1 \\ 1 \\ -2 \end{bmatrix},\ \hat{e}_b = \frac{1}{\sqrt{2}}\begin{bmatrix} -1 \\ 1 \\ 0 \end{bmatrix},\ \hat{e}_{c^*} = \frac{1}{\sqrt{3}}\begin{bmatrix} 1 \\ 1 \\ 1 \end{bmatrix}. \quad (6)$$

This allows us to switch from the spin components along a and b in Eq. (5) to the spin components along x, y and z, which are appropriate for the Kitaev model. Taking into account also the isotropy of the Kitaev model, i.e., $\langle S_1^x(t)S_1^x\rangle = \langle S_1^y(t)S_1^y\rangle = \langle S_1^z(t)S_1^z\rangle$ and similar for the correlation functions $\langle S_1^x(t)S_2^x\rangle$ and $\langle S_2^x(t)S_2^x\rangle$, Eq. (5) simplifies to

$$T_1^{-1} = \frac{1}{2}\gamma^2 A^2 \int_{-\infty}^{\infty} \mathrm{d}t \left\{ 4\big\langle S_1^x(t)S_1^x\big\rangle + \right. \\ \left. + \frac{4}{3}\big\langle S_1^x(t)S_2^x\big\rangle \right\}. \quad (7)$$

Two terms under the integral represent precisely the on-site and NN-sites contributions with the weights 4 and 4/3, respectively. A similar calculation for the magnetic field applied along a or b gives the same result. The theoretical curve plotted in Fig. 2a is based on these weights. As the curves for the on-site and NN-sites contributions are almost identical up to T_H [27], the values of the weights do not affect the form of Eq. (1).

T_1^{-1} in the classical paramagnetic state. In this state, NN spins are not correlated, so that only the on-site spin correlations contribute to T_1^{-1}. A contribution of the correlation function $\langle S_1^x(t)S_1^x\rangle$ amounts to $T_{1x}^{-1} = \sqrt{\pi}\gamma^2 A^2\hbar/(4J\sqrt{z})$ [43], where $\gamma/(2\pi)$ is nuclear gyromagnetic ratio (4.17 MHz/T for ^{35}Cl), J is the exchange coupling (in this case $J_K = 183$ K, as determined in Fig. 1c) and z is the number of neighboring spins with the relevant component of the coupling (x in this case, $z = 1$ for the Kitaev honeycomb lattice). Using Eq. (7), we then obtain $T_1^{-1} = 4T_{1x}^{-1} = \sqrt{\pi}\gamma^2 A^2\hbar/J_K$, which evaluates to 92 s^{-1} using $A = 1.35$ T determined above from Supplementary Fig. S4. This value is consistent with the observed values of 121 s^{-1} and 146 s^{-1} above 120 K (Fig. 2c) for $\vartheta = 0°$ and $\vartheta = 90°$, respectively. In addition, these temperature-independent values are reached at around $2T_H$ ($T_H = 0.375J_K \approx 70$ K), precisely as in the theoretical dataset in Fig. 2a. Both these conclusions demonstrate that the classical paramagnetic state is indeed reached.

T_1 relaxation due to gapped magnons. When spin fluctuations in the magnetic lattice are due to excited magnons, the corresponding spin-lattice relaxation rate for a single-magnon process is given by [44]

$$T_1^{-1} \propto \int g^2(E) f(E)\big[1 + f(E)\big]\mathrm{d}E, \quad (8)$$

where E is the energy of magnons, $g(E)$ is their density of states, $f(E) = [\exp(\beta E) - 1]^{-1}$ is the Bose-Einstein distribution function, $\beta = 1/(k_B T)$, and k_B is the Boltzmann constant. Denoting the magnon gap by Δ (in kelvin units), we define $\varepsilon = E - k_B\Delta$ as the energy measured from the bottom of the magnon band. The power-law dispersion relation $\varepsilon \propto k^s$ in D dimensions, which includes the standard parabolic dispersion ($s = 2$) and the Dirac dispersion ($s = 1$) as special cases, leads to $g(E) \propto \varepsilon^{D/s-1}$. For low temperatures $T \ll \Delta$, the distribution function $f(E)$ can be approximated by the Boltzmann distribution, $f(E) \approx \exp(-\beta E) = \exp(-\Delta/T)\exp(-\beta\varepsilon)$. Plugging these expressions for $g(E)$ and $f(E)$ into Eq. (8), we obtain

$$T_1^{-1} \propto T^{2D/s-1}\exp\left(-\frac{\Delta}{T}\right)\int_0^{\infty} \exp(-x)\, x^{2(D/s-1)}\,\mathrm{d}x. \quad (9)$$

The integral on the right side of Eq. (9) converges if $s < 2D$ and evaluates to $\Gamma(2D/s - 1)$ where Γ is the gamma function. We can thus rewrite Eq. (9) as

$$T_1^{-1} \propto T^p \exp\left(-\frac{\Delta}{T}\right) \quad (10)$$

with the power of the prefactor $p = 2D/s - 1$. In case of $D = 2$, which is relevant for the Kitaev honeycomb magnet, $p = 1$ for $s = 2$ and $p = 3$ for $s = 1$, so that the power p cannot be negative. Even in case of $D = 1$, p can only approach the lowest value of 0 precisely for $s = 2$ (although care should be taken in this case, as the integral in Eq. (9) then formally diverges). If more than a single magnon is involved in the T_1 process, the power p is also positive and becomes even higher [44]. Gapped magnons thus cannot lead to the T_1 relaxation described by Eq. (10) with $p < 0$, which is the case in Eq. (1).

Instead, we can use Eq. (9) in the 3D magnetically ordered state, when the elementary excitations are magnons with a gap Δ_m. In this case $D = 3$ and $s = 2$, and this leads to $T_1^{-1} \propto T^2\exp(-\Delta_m/T)$. We use this expression to analyze the $T_1^{-1}(T)$ data (Fig. 2c) in the low-temperature ordered state of α-$RuCl_3$.

All these examples show that a frequently used simple gapped model $T_1^{-1} \propto \exp(-\Delta_s/T)$ with the gap Δ_s, which was used before to analyze the $T_1^{-1}(T)$ datasets in α-$RuCl_3$ [32], is actually not justified in any region of the phase diagram of α-$RuCl_3$.

Majorana fermion gap. In the presence of an external magnetic field, Majorana fermions in the Kitaev model acquire a gap [2]. This is shown for a field applied perpendicularly to the honeycomb plane, i.e., in the $(1,1,1)$ direction in the coordinate system defined by the Kitaev axes x, y and z. In this case, the Zeeman term reads $\mathcal{H}_Z = -h\sum_j (S_j^x + S_j^y + S_j^z)$, where $h = g\mu_B B/\sqrt{3}$ is a single component of the magnetic field B in energy units, g is the g-factor and μ_B is the Bohr magneton. When treated as a perturbation to the Kitaev Hamiltonian, the Zeeman term contributes to the Majorana fermion gap only at third order [2]. The corresponding effective Hamiltonian is thus proportional to h^3 and can be written as [2, 4, 5]

$$\mathcal{H}_{\text{eff}}^{(3)} = -3\alpha \frac{h^3}{k_B^2 \Delta_0^2} \sum_{jkl} S_j^x S_k^y S_l^z, \tag{11}$$

where Δ_0 is the two-flux gap (in kelvin units), while α (of the order of unity) accounts for the sum over the excited states, and its exact value is not known. The Kitaev model extended with such a three-spin exchange term $-\kappa \sum_{jkl} S_j^x S_k^y S_l^z$ with $\kappa = 3\alpha h^3/(k_B^2\Delta_0^2)$ is still exactly solvable and the dispersion relation of the Majorana fermions is calculated as [4]

$$E_{\mathbf{k}} = 2\sqrt{k_B^2 J_K^2 |1 + e^{i\mathbf{k}\cdot\mathbf{a}_1} + e^{i\mathbf{k}\cdot\mathbf{a}_2}|^2 + \kappa^2 \sin^2(\mathbf{k}\cdot\mathbf{a}_1)}, \tag{12}$$

where J_K is the Kitaev coupling (in kelvin units), while $\mathbf{a}_1$ and $\mathbf{a}_2$ are the base vectors of the honeycomb lattice. The dispersion relation given by Eq. (12) is gapped for $\kappa \neq 0$, and the corresponding gap Δ_f can be calculated numerically as a function of κ and thus as a function of the magnetic field. For small magnetic fields, i.e., for $\kappa \ll k_B J_K$, the Majorana fermion gap (in kelvin units) simplifies to

$$\Delta_f = \sqrt{3}\frac{\kappa}{k_B} = \frac{\alpha}{\Delta_0^2}\left(\frac{g\mu_B B}{k_B}\right)^3, \tag{13}$$

while for high magnetic fields it saturates to $\Delta_f = 2J_K$. The total spin-excitation gap Δ is obtained by adding Δ_f to the two-flux gap Δ_0 as in Eq. (2). The whole field dependence of Δ is shown in Supplementary Fig. S8 for $J_K = 183$ K as determined in Fig. 1c, $g = g_{ab}$ and $\alpha = 1.2$ (leading to the best fit of our $\Delta(B_{ab})$ data points). The cubic approximation given by Eq. (13), which is plotted in Fig. 1c and, for comparison, also in Supplementary Fig. S8, is apparently valid up to 15 T, well beyond the field range covered in this work.

Data availability. The data that support the plots within this paper and other findings of this study are available from the corresponding author upon reasonable request.

* martin.klanjsek@ijs.si

[39] A. Abragam, Principles of Nuclear Magnetism, Oxford University Press, Oxford (2011).

[40] M. Jeong, H. Mayaffre, C. Berthier, D. Schmidiger, A. Zheludev, and M. Horvatić, Attractive Tomonaga-Luttinger Liquid in a Quantum Spin Ladder, *Phys. Rev. Lett.* **111**, 106404 (2013).

[41] M. Klanjšek, D. Arčon, A. Sans, P. Adler, M. Jansen, and C. Felser, Phonon-Modulated Magnetic Interactions and Spin Tomonaga-Luttinger Liquid in the p-Orbital Antiferromagnet CsO_2, *Phys. Rev. Lett.* **115**, 057205 (2015).

[42] M. Horvatić and C. Berthier, "NMR Studies of Low-Dimensional Quantum Antiferromagnets," in C. Berthier, L. P. Levy, and G. Martinez, *High Magnetic Fields: Applications in Condensed Matter Physics and Spectroscopy* (Springer-Verlag, Berlin, 2002), p. 200.

[43] T. Moriya, Nuclear Magnetic Relaxation in Antiferromagnetics, *Prog. Theor. Phys.* **16**, 23-44 (1956).

[44] D. Beeman and P. Pincus, Nuclear Spin-Lattice Relaxation in Magnetic Insulators, *Phys. Rev.* **166**, 359-375 (1968).

SUPPLEMENTARY INFORMATION

to "Observation of two types of fractional excitations in the Kitaev honeycomb magnet" by Nejc Janša *et al.*

Magnetic susceptibility

Magnetic susceptibility measurements of α-$RuCl_3$ were performed using a Quantum Design MPMS. A powdered sample of the mass 22.5 mg was placed into a plastic capsule, in a glovebox to avoid contact with air, and then quickly transferred into the MPMS. Fig. S1 shows the measured susceptibility taken with cooling in field and in zero field. The obtained curve with the magnetic transition at $T_{N2} = 14$ K (inset of Fig. S1) is almost identical to the corresponding curve in Ref. [S1].

Nuclear magnetic resonance

Orientation dependence of the NMR spectrum. The ^{35}Cl nuclear magnetic resonance (NMR) spectra were recorded point by point in frequency steps of 50 or 100 kHz, so that the Fourier transform of the signal was integrated at each step to arrive at the individual spectral point. The covered NMR frequency range was from 34 MHz, the lower limit of our setup, up to 50 MHz. The dependence of the corresponding part of the NMR spectrum on the direction of the external magnetic field of 9.4 T (described by the angle ϑ from the crystal ab plane) at a temperature of 20 K is shown in Fig. S2. The spectra are extremely broad because of a large ^{35}Cl (with $I = 3/2$ spin) quadrupole interaction. As concluded in Methods, a large portion of the covered frequency range is associated with the central, $1/2 \longleftrightarrow -1/2$ ^{35}Cl NMR transition. As this transition is observed to consist of at least three peaks (Fig. S2), even for the symmetric $\vartheta = 90°$ orientation, while there are only two inequivalent Cl sites in the crystal structure, the splitting of the central line is likely a consequence of stacking faults in the layered crystal structure or crystal twinning, or both.

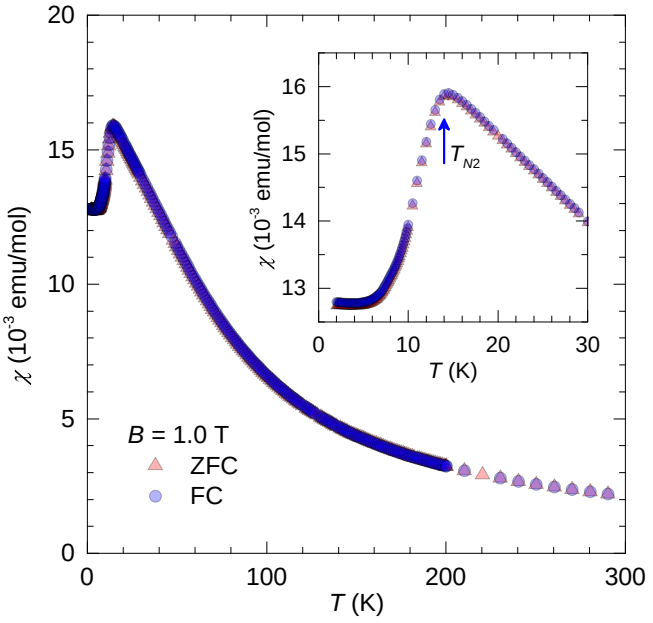

FIG. S1: **Magnetic susceptibility.** Zero-field-cooled (ZFC) and field-cooled (FC) magnetic susceptibility of the powdered α-$RuCl_3$ sample in a magnetic field of 1.0 T. Inset is a blow-up around the magnetic phase transition at $T_{N2} = 14$ K.

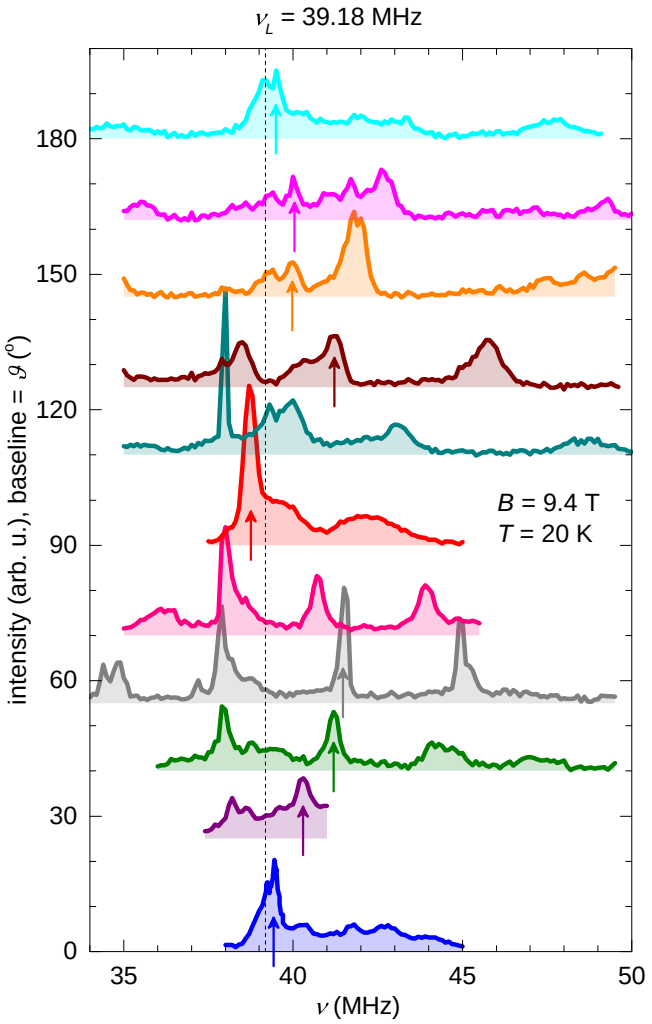

FIG. S2: **Orientation dependence of the NMR spectrum.** Central line of the ^{35}Cl NMR spectrum of the α-$RuCl_3$ single crystal taken at 20 K in the field of 9.4 T applied at an angle ϑ with respect to the crystal ab plane (as shown in Fig. 1a). The plane of rotation is at an angle of 15° from the crystal b axis (as shown in Fig. 1a). Dashed vertical line indicates the Larmor frequency ν_L. Arrows mark the peak whose temperature dependence is analyzed in Fig. S3 and where T_1 displayed in Fig. 3 was measured. The $\vartheta = 180°$ spectrum corresponds to the only field direction outside the red fan in Fig. 1a.

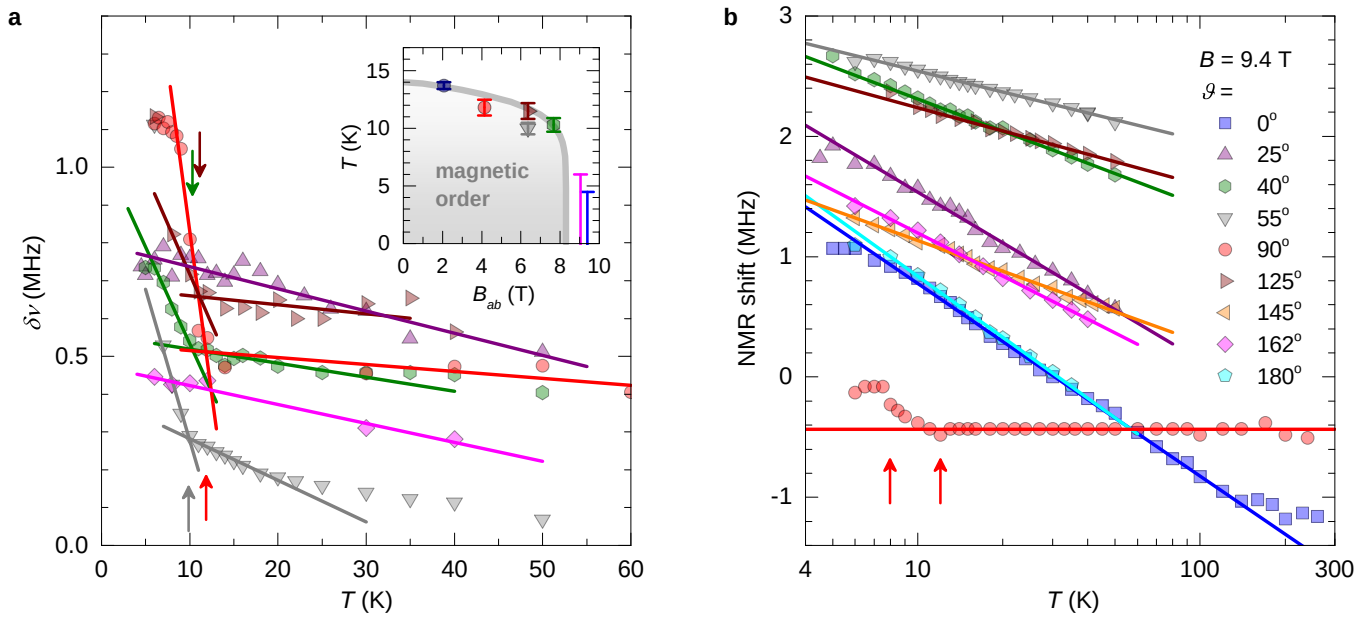

FIG. S3: **Temperature dependence of the NMR line.** The temperature (T) dependence of **a**, the width $\delta\nu$, and **b**, the NMR shift of dominant ^{35}Cl NMR peaks (marked by arrows in Fig. S2) in 9.4 T ($\nu_L = 39.18$ MHz for ^{35}Cl) for various sample orientations given by ϑ. The overlaping peaks for some values of ϑ do not allow the determination of $\delta\nu$. For each dataset drawn in **a**, straight lines are linear fits on both sides of the kink at T_{N2} (determined as the temperature of intersection and marked by an arrow) indicating the onset of low-temperature magnetic ordering. Inset shows the obtained points of the phase boundary (same symbols as the corresponding $\delta\nu(T)$ datasets) compared to the result of Ref. [S1] (gray line). Straight lines in **b** are phenomenological $\log T$ fits. Only the $\vartheta = 90°$ dataset in **b** shows signs of magnetic transitions (marked by arrows).

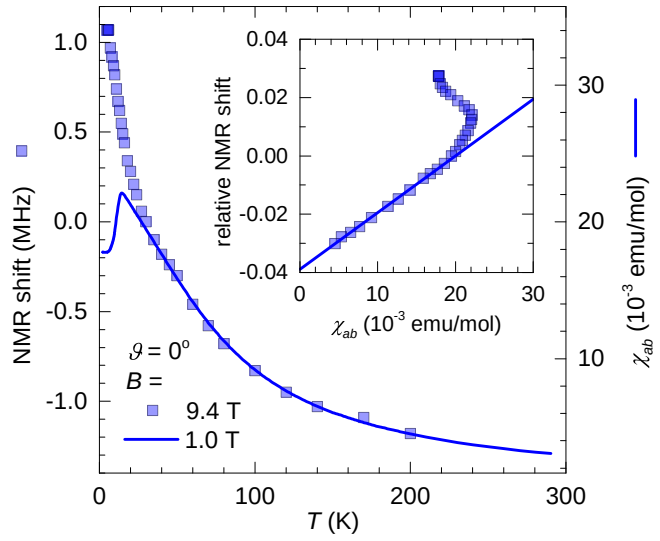

FIG. S4: **NMR shift against susceptibility.** Temperature dependencies of the ^{35}Cl NMR shift of the dominant NMR peak measured in 9.4 T with the field in the ab plane ($\vartheta = 0°$) and magnetic susceptibility χ_{ab} are proportional to each other down to 35 K. Inset shows the dependence of the relative NMR shift (i.e., NMR shift divided by $\nu_L = 39.18$ MHz) on χ_{ab}. Line is a linear fit of the dataset up to $20 \cdot 10^{-3}$ emu/mol, i.e., down to 35 K, leading to the component $A = 1.35$ T (in the ab plane) of the hyperfine coupling tensor between ^{35}Cl and the Ru^{3+} $S = 1/2$ spin, as described in Methods.

Temperature dependence of the NMR line. We measured the temperature dependence of the dominant ^{35}Cl NMR peak in a field of 9.4 T for various sample orientations with respect to the magnetic field direction. From these measurements, we determined the temperature dependence of the frequency width (Fig. S3a) and the NMR shift of the peak with respect to the Larmor frequency (Fig. S3b). For $B_{ab} < 8$ T, the width exhibits a clear kink as a function of temperature, which indicates the onset of NMR line broadening at the phase transition into the magnetically ordered state. Plotting the temperature of the kink as a function of B_{ab} in the inset of Fig. S3 (and in Fig. 1b), we obtain the phase boundary of the magnetically ordered state, which perfectly matches the result of the reference study [S1]. In contrast, the NMR shift does not exhibit any signs of a magnetic transition, except for the $\vartheta = 90°$ dataset. We find the NMR shift to be a monotonic function of temperature T, empirically following a $\log T$ dependence over a broad temperature range.

Contributions to the NMR shift. Fig. S4 shows the temperature dependence of the frequency shift of the dominant NMR peak taken in 9.4 T for $\vartheta = 0°$ (Fig. S3b), i.e., with the field in the ab plane. Its comparison to the rescaled magnetic susceptibility χ_{ab} allows us to separate the magnetic contribution to the NMR shift from the temperature-independent quadrupole contribution.

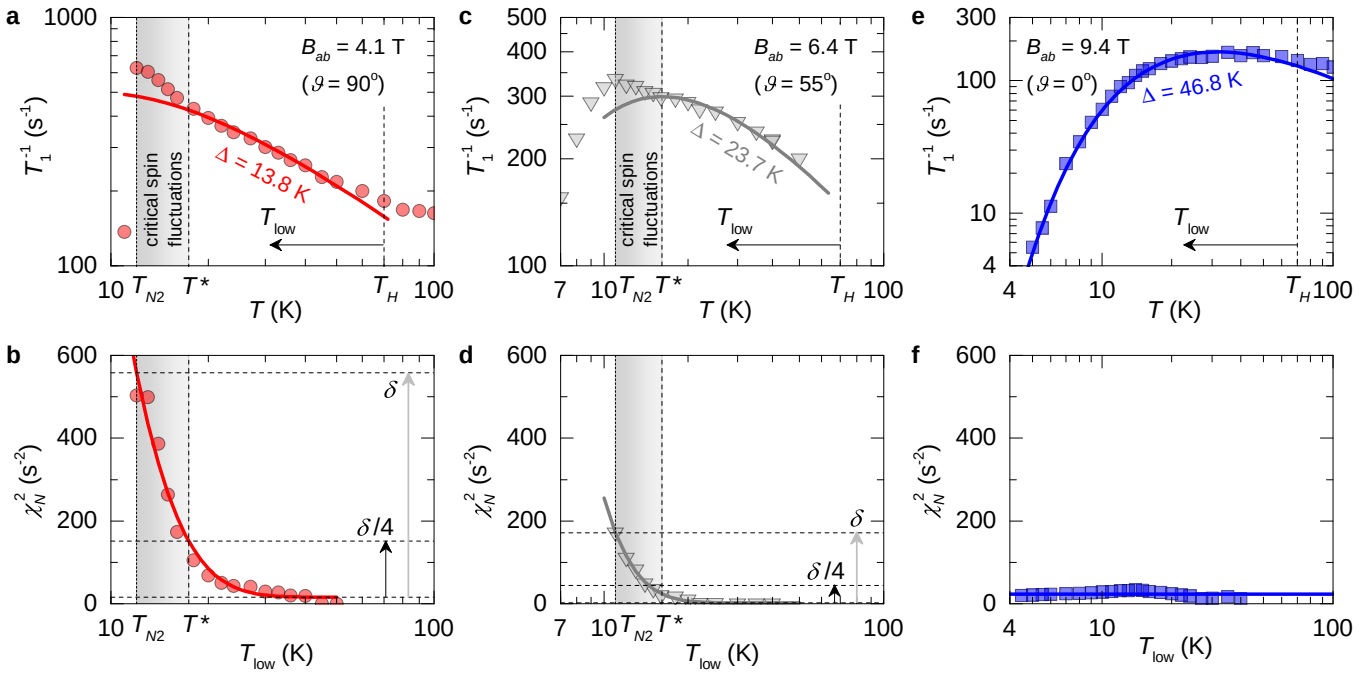

FIG. S5: **Determination of the onset temperature T^* for the critical spin fluctuations. a,c,e**, The representative ^{35}Cl $T_1^{-1}(T)$ datasets from Fig. 3 taken in 9.4 T for $\vartheta = 90°$, 55° and 0°. Solid lines are fits to Eq. (1) with $n = 0.67$ in the temperature range between T^*, where the critical spin fluctuations (gray) related to magnetic ordering at T_{N2} vanish, and $T_H \approx 70$ K. **b,d,f**, The $T_1^{-1}(T)$ datasets in **a**, **c** and **e** are fitted with Eq. (1) in the temperature range between the varying $T_{\rm low} < T_H$ and T_H (so that the fitting range contains at least three data points), and the goodness of the fit χ^2_N (normalized to the number N of involved data points) is plotted as a function of $T_{\rm low}$. Solid lines are fits with the phenomenological function $\chi^2_N = a\exp(-\kappa T_{\rm low}) + b$. T^* is defined as the temperature where the χ^2_N fit (measured from the base line) reaches 1/4 of the maximum value δ reached at T_{N2}. The dataset for $\vartheta = 0°$ exhibits no magnetic ordering (**e**) and thus no critical spin fluctuations (**f**).

Determination of the onset temperature T^*. To determine the onset temperature T^* for the critical spin fluctuations preceding the magnetic ordering at T_{N2}, we apply the following procedure to the selected $T_1^{-1}(T)$ dataset. We fit a part of the dataset between $T_H = 0.375J_K \approx 70$ K (for $J_K = 190$ K [S4]) and the varying temperature $T_{\rm low} < T_H$, which contains at least three data points, to Eq. (1) with $n = 0.67$ for Kitaev spin fluctuations. Then we plot the goodness of the fit χ^2_N (normalized to the number N of involved data points) as a function of $T_{\rm low}$. As shown in Fig. S5 for the representative ^{35}Cl $T_1^{-1}(T)$ datasets from Fig. 3, χ^2_N is almost constant down to some temperature, and then starts to rapidly increase as $T_{\rm low}$ approaches the magnetic ordering temperature T_{N2}. This rise indicates that the fitting range starts to progressively cover the data points that do not follow Eq. (1) anymore, meaning that they already reflect the critical spin fluctuations preceding the magnetic ordering at T_{N2}. The $\chi^2_N(T_{\rm low})$ datasets can be nicely fitted to a phenomenological function $\chi^2_N = a\exp(-\kappa T_{\rm low}) + b$ where a, b and κ are the fitting parameters. We define T^* as the temperature where the χ^2_N fit (measured from the base line) reaches 1/4 of the maximum value reached at T_{N2}, as shown in Figs. S5b and d. Comparing Figs. S5b, d and f, we see that the critical spin fluctuations weaken with increasing B_{ab}, i.e., when moving towards the critical magnetic field $B_c \approx 8$ T in the phase diagram in Fig. 1b, and disappear above B_c, just as expected.

Gap value across the NMR spectrum. As the values of the hyperfine coupling constant A are different for different NMR peaks, T_1^{-1}, which is proportional to A^2, is expected to vary across the NMR spectrum. The question then arises whether there is any variation of the determined spin-excitation gap Δ across the NMR spectrum. Fig. S6 shows the determination of Δ on various ^{35}Cl NMR peaks for selected orientations ϑ in 9.4 T. Although the $T_1^{-1}(T)$ datasets taken on different peaks are significantly offset with respect to each other on the logarithmic scale, as expected, the obtained Δ shows only a negligible variation across the NMR spectrum. This is actually expected, as Δ is related only to the underlying Kitaev physics and should not depend on the coupling constants.

Choice of the g-tensor eigenvalues. While there is a consensus regarding the value of $g_{ab} = 2.5$ in the lit-

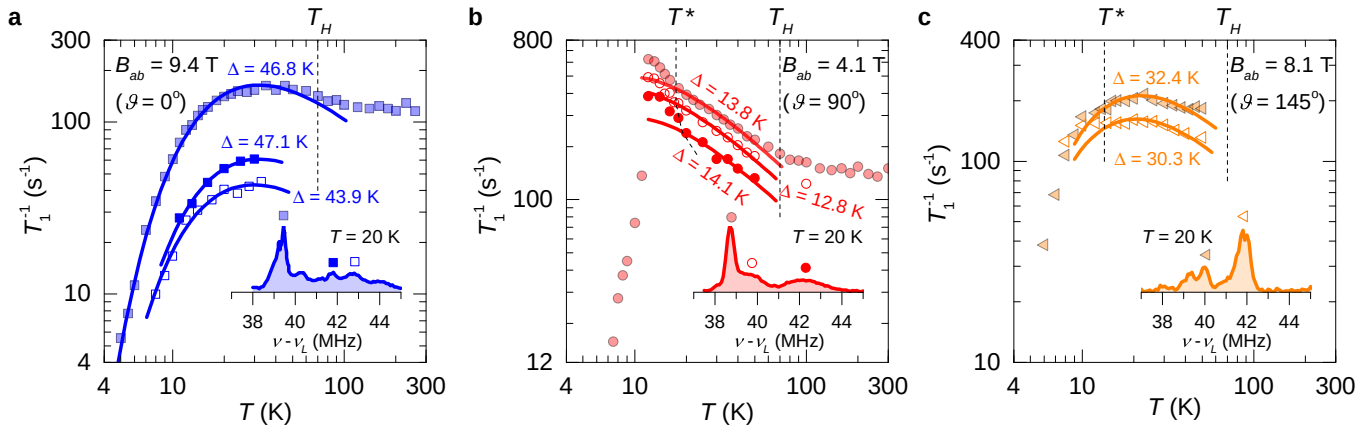

FIG. S6: **Gap values on different NMR peaks. a-c**, The $T_1^{-1}(T)$ datasets taken on different ^{35}Cl NMR peaks (marked with the corresponding symbols in the insets, which show the NMR spectra) in 9.4 T for selected orientations ϑ (and hence B_{ab}). To obtain the gap value Δ for different NMR peaks, each dataset is fitted with Eq. (1) between T^*, determined as shown in Fig. S5, and $T_H = 70$ K.

erature [S2, S3], the value of g_{c^*} was first estimated to 0.4 in Ref. [S2] and then refined to 1.1 in Ref. [S3] based on theoretical calculations. As the theoretical result also fits perfectly to the magnetization curves from Ref. [S1], the corresponding g_{c^*} value is definitely more reliable. Nevertheless, to see the dependence of our conclusions on the choice of the g_{c^*} value, we repeat the analysis of the field dependence of the spin-excitation gap Δ from Fig. 1c, where we assumed $g_{c^*} = 1.1$, also with the alternative value $g_{c^*} = 0.4$. As shown in Fig. S7, the two datasets differ only a little, so that the obtained values $J_K = 183$ K and 212 K of the Kitaev exchange coupling are both in agreement with the recent determination of $J_K = 190$ K in Ref. [S4]. Our conclusions are thus essentially independent of the choice of the g_{c^*} value.

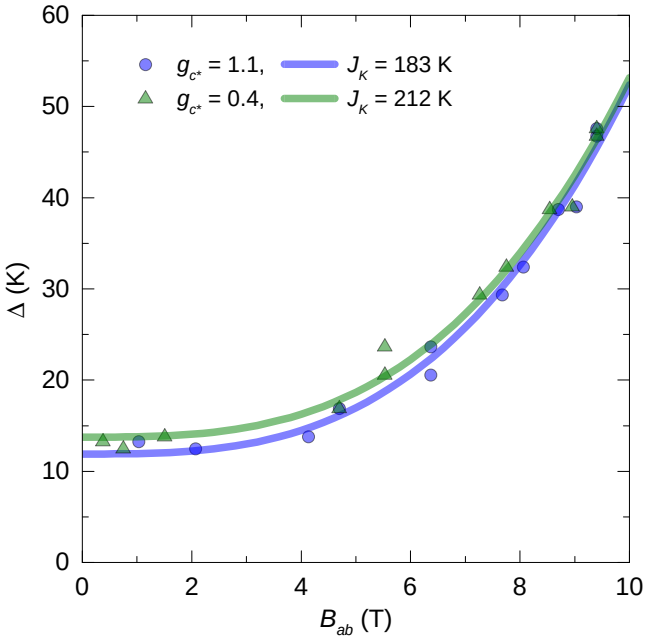

FIG. S7: **Choice of the g_{c^*} value.** The spin-excitation gap Δ as a function of B_{ab} for two different choices of g_{c^*}. The choice $g_{c^*} = 1.1$ is used in the main text. Solid lines are fits with Eq. (2).

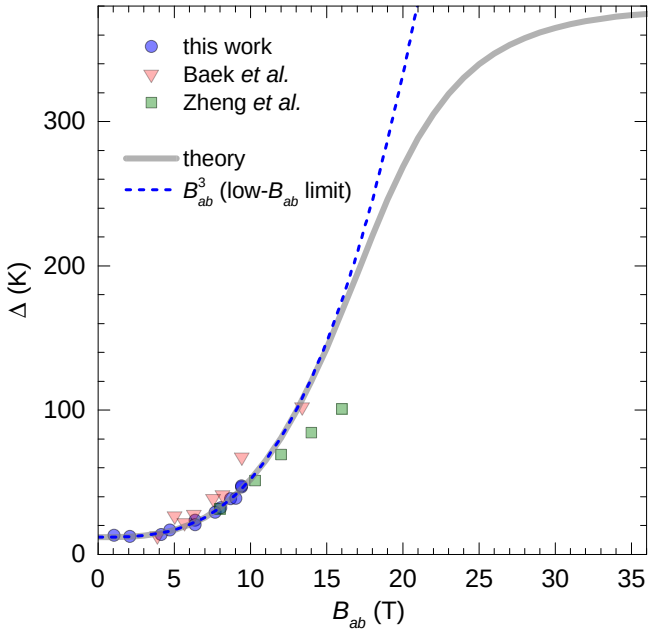

FIG. S8: **Spin-excitation gap.** The spin-excitation gap Δ as a function of the magnetic field B_{ab} obtained from $T_1^{-1}(T)$ data in our work and in two recent works [S5, S6] using our model given by Eq. (1). The data are compared to the full theoretical expression described in Methods (using $J_K = 183$ K determined in Fig. 1c, $\alpha = 1.2$, $g = g_{ab}$), which simplifies to the B_{ab}^3 dependence given by Eq. (2) (i.e., Δ_0 added to Δ_f in Eq. (13)) in the low-field region.

Comparison with recent works

Recent NMR measurements. Very recently, two ^{35}Cl NMR studies of α-$RuCl_3$ appeared [S5, S6]. The analysis of both studies is focused on the low-temperature region below 15 K. Using a simple exponential model $T_1^{-1} \propto \exp(-\Delta_s/T)$ in this region, Ref. [S5] finds that the spin-excitation gap Δ_s opens linearly with the field above the critical field of around 10 T. On the other hand, Ref. [S6] extends the covered temperature range down to 1.5 K and finds a low-temperature gapless, power-law behavior of $T_1^{-1}(T)$ in the covered high-field region above the critical field of around 8 T.

As these conclusions are very different from our own, also because of a quite different data analysis, we reanalyze the $T_1^{-1}(T)$ datasets obtained in these two works also with our theoretically verified model given by Eq. (1). As in our work, we focus on the Kitaev paramagnetic region, i.e., on the temperature range from $T_H = 70$ K down to the onset of critical fluctuations related to magnetic ordering below 8 T, and down to 4.2 K above 8 T (or a bit higher at higher fields), including the characteristic maximum in $T_1^{-1}(T)$ as the main feature. The data in Ref. [S6] were taken with a field applied in the crystal ab plane, while the data in Ref. [S5] were taken with a field applied at 30° and −60° with respect to the ab plane. In this case, we calculate the effective field values B_{ab} in the same way as in our work. The obtained field dependence of the excitation gap $\Delta(B_{ab})$ for both works is shown in Fig. S8 together with our result. Applying our analysis to the data from all three works apparently leads to relatively consistent results. Nevertheless, the results for the data from Refs. [S5, S6] alone do not allow us to make any conclusions about the cubic field dependence of Δ, mostly due to the lack of important low-field data points. Regarding Ref. [S6], the obtained $\Delta(B_{ab})$ data points, which complement our field region, nicely continue the trend set by our data points. The obtained trend is approximately linear in field, consistent with the theoretical prediction in this intermediate-field region, although with a different slope. As the theoretical prediction is based on a perturbative treatment, it is not surprising that it might not give reliable results outside the low-field region.

In light of our conclusions, the reported findings of these two works should be understood in the following way. While the true signs of fractionalization into Majorana fermions and gauge fluxes can be found in the Kitaev paramagnetic region covering a broad temperature range up to around 100 K (Fig. 1b), the physics at low temperatures of the order of 10 K and below is apparently obscured by the effect of inevitable non-Kitaev interactions, as predicted already in Ref. [S6].

Recent specific-heat measurements. The magnetic field dependence of the spin-excitation gap was recently determined also from the temperature dependence of the specific heat above the critical magnetic field of around 8 T [S7]. Using a simple exponential model $C_m \propto \exp(-\Delta_{\mathrm{Sears}}/T)$ for the magnetic contribution to the specific heat C_m in the low-temperature region, the authors concluded on a linear opening of the gap Δ_{Sears} with the field B_{ab} above the critical field, in an attempt to show the consistency with the $d = 2$ Ising model. However, a careful look at the $\Delta_{\mathrm{Sears}}(B_{ab})$ dataset, shown in Fig. S9, reveals a clear convex shape, which can be nicely fitted with the cubic B_{ab}^3 dependence with a finite zero-field value, in accordance with Eq. (2). As the Δ_{Sears} values in Ref. [S7] were obtained using a simple fitting model different from our theoretically verified model in Eq. (1), this result cannot be directly compared to our own $\Delta(B_{ab})$ dataset from Fig. 1c. For the purpose of comparison, we rescale the $\Delta_{\mathrm{Sears}}(B_{ab})$ dataset in Fig. S9 to match our $\Delta(B_{ab})$ dataset at 9 T. The datasets can then be considered consistent with each other, where the B_{ab}^3 fits of both yield consistent zero-field values.

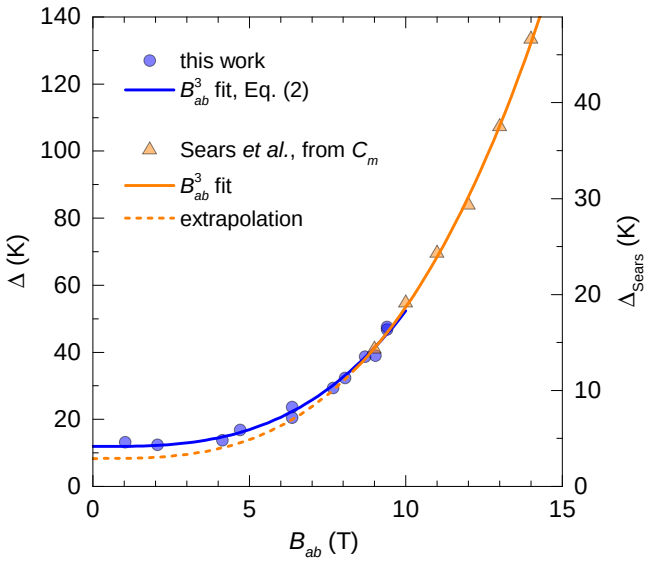

FIG. S9: **Spin-excitation gap from the specific heat.** The spin-excitation gap Δ as a function of the magnetic field B_{ab} from Fig. 1c compared to the $\Delta(B_{ab})$ dataset obtained from the specific-heat measurements in Ref. [S7] (scale Δ_{Sears} on the right vertical axis) rescaled to match our dataset at 9 T (scale Δ on the left vertical axis). Blue line is a theoretical B_{ab}^3 curve given by Eq. (2) (using $J_K = 183$ K determined in Fig. 1c, $\alpha = 1.2$, $g = g_{ab}$), solid orange line is a B_{ab}^3 fit of the specific-heat $\Delta(B_{ab})$ dataset and dashed orange line is its extrapolation to the low-field region.

[S1] R. D. Johnson, S. C. Williams, A. A. Haghighirad, J. Singleton, V. Zapf, P. Manuel, I. I. Mazin, Y. Li, H. O. Jeschke, R. Valentí, and R. Coldea, Monoclinic crystal

structure of α-$RuCl_3$ and the zigzag antiferromagnetic ground state, *Phys. Rev. B* **92**, 235119 (2015).

[S2] Y. Kubota, H. Tanaka, T. Ono, Y. Narumi, and K. Kindo, Successive magnetic phase transitions in α-$RuCl_3$: XY-like frustrated magnet on the honeycomb lattice, *Phys. Rev. B* **91**, 094422 (2015).

[S3] R. Yadav, N. A. Bogdanov, V. M. Katukuri, S. Nishimoto, J. van den Brink, and L. Hozoi, Kitaev exchange and field-induced quantum spin-liquid states in honeycomb α-$RuCl_3$, *Sci. Rep.* **6**, 37925 (2016).

[S4] S.-H. Do, S.-Y. Park, J. Yoshitake, J. Nasu, Y. Motome, Y. S. Kwon, D. T. Adroja, D. J. Voneshen, K. Kim, T.-H. Jang, J.-H. Park, K.-Y. Choi, and S. Ji, Majorana fermions in the Kitaev quantum spin system α-$RuCl_3$, *Nature Phys.* **13**, 1079 (2017).

[S5] S.-H. Baek, S.-H. Do, K.-Y. Choi, Y. S. Kwon, A. U. B. Wolter, S. Nishimoto, J. van den Brink, and B. Büchner, Evidence for a Field-induced Quantum Spin Liquid in α-$RuCl_3$, *Phys. Rev. Lett.* **119**, 037201 (2017).

[S6] J. Zheng, K. Ran, T. Li, J. Wang, P. Wang, B. Liu, Z.-X. Liu, B. Normand, J. Wen, and W. Yu, Gapless Spin Excitations in the Field-Induced Quantum Spin Liquid Phase of α-$RuCl_3$, *Phys. Rev. Lett.* **119**, 227208 (2017).

[S7] J. A. Sears, Y. Zhao, Z. Xu, J. W. Lynn, and Y.-J. Kim, Phase diagram of α-$RuCl_3$ in an in-plane magnetic field, *Phys. Rev. B* **95**, 180411(R) (2017).